Journal of Power Sources 644 (2025) 237136

Contents lists available at ScienceDirect

Journal of Power Sources

journal homepage: www.elsevier.com/locate/jpowsour

Chemo-thermal stress in all-solid-state batteries: Impact of cathode active materials and microstructure

Fadi Al-Jaljouli [a,b,*], Robert Mücke [a], Christoph Roitzheim [a], Yoo Jung Sohn [a], Najma Yaqoob [a,d], Martin Finsterbusch [a,e], Payam Kaghazchi [a,d], Olivier Guillon [a,b,c,e]

[a] Forschungszentrum Jülich GmbH, Institute of Energy Materials and Devices, Materials Synthesis and Processing (IMD-2), 52425, Jülich, Germany
[b] Institute of Mineral Engineering, RWTH Aachen University, 52064, Aachen, Germany
[c] Jülich Aachen Research Alliance: JARA-Energy, Jülich, 52425, Germany
[d] MESA+ Institute for Nanotechnology, University of Twente, P. O. Box 217, Enschede, 7500AE, the Netherlands
[e] Helmholtz Institute Munster: Ionics in Energy Storage (IMD-4 / HI MS), Munster, 48149, Germany

HIGHLIGHTS

- Chemo-thermal stress includes thermal and chemical stresses.
- Thermal stress significantly impacts Chemo-thermal stress in ASSBs.
- LCO shows ~43 % lower chemo-thermal stress than chemical stress.
- $Li_{0.5}$NCM955 and $Li_{0.1}$NCM955 show ~42 % and ~15 % higher chemo-thermal stresses.
- CAM volume change is not a reliable indicator of mechanical stress levels.

ARTICLE INFO

Keywords:
All-solid-state lithium batteries
Thermal stress
Chemo-thermal stress
Composite cathodes
Microstructural design parameters

ABSTRACT

The transition from conventional lithium-ion to all-solid-state lithium batteries (ASSBs) promises enhanced safety and higher energy density but also gives rise to new challenges, like capacity degradation due to enhanced mechanical stresses. This study addresses the often-overlooked residual (thermal) mechanical stress arising during manufacturing, which can significantly contribute to the overall mechanical stress. While stress evolution during battery operation is often only associated with the de-/lithiation-induced stresses from the active material, we introduce a "chemo-thermal stress" description. By this integration of thermal and chemical stresses, we developed a more accurate level to simulate real-life conditions, especially for all-solid-state batteries. This holistic approach demonstrated for the first time, that thermal stresses from manufacturing can reduce the induced mechanical stress in $LiCoO_2$ (LCO) during delithiation, resulting in the total chemo-thermal stress being approximately 43 % lower. In contrast, residual thermal stress exacerbates chemical stress in $Li_{0.5}$NCM955 and $Li_{0.1}$NCM955, leading to a principal stress increases of approximately 42 % and 15 %, respectively. We also examine the impact of microstructural design parameters, particularly the solid volume fraction of the cathode active material (CAM) and relative density, on the induced mechanical stresses within CAM and the solid electrolyte (SE). Our investigation reveals that the volume change in cathode active materials, a primary contributor to induced mechanical stress in ASSBs, is not a reliable factor for predicting final stresses in actual full battery cells. Additionally, our findings highlight LCO's superior mechanical behavior compared to $Li_{0.5}$NCM955 and $Li_{0.1}$NCM955, attributed to lower overall stress and prevalent compressive stress, which mitigates failure risks in oxide materials.

* Corresponding author. Forschungszentrum Jülich GmbH, Institute of Energy Materials and Devices, Materials Synthesis and Processing (IMD-2), 52425, Jülich, Germany.
E-mail addresses: f.al-jaljouli@fz-juelich.de (F. Al-Jaljouli), r.muecke@fz-juelich.de (R. Mücke), c.roitzheim@fz-juelich.de (C. Roitzheim), y.sohn@fz-juelich.de (Y.J. Sohn), n.yaqoob@fz-juelich.de (N. Yaqoob), m.finsterbusch@fz-juelich.de (M. Finsterbusch), p.kaghazchi@fz-juelich.de (P. Kaghazchi), o.guillon@fz-juelich.de (O. Guillon).

https://doi.org/10.1016/j.jpowsour.2025.237136
Received 8 February 2025; Received in revised form 8 April 2025; Accepted 19 April 2025
Available online 26 April 2025

1. Introduction

The transition from liquid lithium-ion batteries (LIBs) to all-solid-state lithium batteries (ASSBs) by replacing the conventional liquid electrolyte with a ceramic, is a promising way to enhance safety and energy density [1–4]. However, challenges such as dendrite formation [5–8], undesirable chemical reactions which occur along the interface between cathode active material (CAM) and solid electrolyte (SE) [9–11], and the mechanical fatigue during cycling results in significant degradation [12–14] persist in impeding the progress of ASSBs. Mechanical stresses induced within the system are primarily due to the rigid constraint imposed by the SE on the volume changes of CAMs [15–17].

CAMs composed of layered transition metal oxides have garnered significant attention from researchers. $LiCoO_2$ (LCO) is renowned for its electrochemical cyclability and high capacity [18–22]. However, LCO is marred by drawbacks stemming from its toxicity and high cost. Furthermore, its inherent structural instability results in a reduced experimental capacity, with a maximum achievable value of 140 mAh/g compared to theoretical 280 mAh/g. [23,24]. This spurred the exploration of nickel-rich materials. Lithium nickel manganese cobalt oxide $LiNi_{1-x-y}Co_xMn_yO_2$ (NCM), is currently regarded as most promising active material attributed to its higher voltage plateau [25,26], higher energy density and lower cost [27–34]. However, it is important to note that during cycling, NCM also generates more heat and is more prone to structural degradation leading to diminished capacity retention [35–38]. Among NCM family, NCM955 is distinguished by its highest specific capacity of 215 mAh/g and affordability. This increased reversible capacity is attributed to its increased nickel content [39].

From the wide variety of solid Li ion conductors, garnet type $Li_7La_3Zr_2O_{12}$ (LLZO) attracts particular attention. LLZO provides a high room temperature ionic conductivity of more than 1 $mScm^{-1}$, low electronic conductivity, broad electrochemical stability window, and a unique chemical and electrochemical stability towards Li metal [40–44]. Stoichiometric LLZO ($Li_7La_3Zr_2O_{12}$) undergoes a volume change during the transition from the tetragonal to the cubic phase, this transition is primarily temperature-dependent. Buschmann et al. observed that a reversible tetragonal-to-cubic transition can be induced upon heating above ~100–150 °C [42]. However, the associated volume change is minimal. Geiger et al. reported that tetragonal $Li_7La_3Zr_2O_{12}$ has lattice parameters a = 13.134(2) Å and c = 12.663(2) Å, while the cubic form has a = 12.943(1) Å, indicating only a slight volumetric variation [45]. Defect generation, such as hydration, can also induce minor volume changes in stoichiometric LLZO. Larraz et al. investigated the effect of hydration on tetragonal LLZO and reported a slight, reversible volume expansion (~0.78 %) when transitioning from the tetragonal phase (2173 $Å^3$) to the cubic phase (2190 $Å^3$) [46]. These minor volume fluctuations can be avoided by doping LLZO with elements such as Al and Ta, which stabilize the cubic phase. Besides a Li metal anode, the cathode will be decisive for the areal capacity and energy density of an ASSB. In order to realize such high energy density ASSBs, a thick composite cathode composed of intertwined SE (LLZO) and CAM particles to provide percolating pathways for ion and electron transport is needed. The fabrication of such LLZO garnet based composite cathodes is challenging. High temperature co-sintering step of SE and CAM at temperatures above 1000 °C is necessary. Material compatibility issues and residual thermal stress are the consequences of the required thermal treatment. The thermodynamic stability issue of LLZO/CAM mixtures was already intensively investigated by several groups [47–54]. Out of the different CAMs known from LIBs, only $LiCoO_2$ (LCO) was shown to be thermodynamically stable in combination with LLZO elevated temperatures, while other CAMs like NCM, $LiNi_{0.8}Co_{0.15}Al_{0.05}O_2$ (NCA), $LiMn_2O_4$ (LMO) and $LiFePO_4$ (LFP) were shown to react already at moderate temperatures between 400 °C and 800 °C.

Significant effort has been devoted to investigate the induced mechanical stress in composite cathodes of ASSBs during delithiation. However, the residual mechanical stress resulting from manufacturing processes, particularly thermal sintering, has often been disregarded. Yet, neglecting this aspect could compromise the accuracy of real-life calculations. In this study, we highlight the critical role of residual mechanical stress resulting from thermal strain mismatch between the CAM and SE during cooling after sintering (thermal stress). This residual stress significantly impacts the overall mechanical stress when combined with the stress induced by the delithiation process (chemical stress). Therefore, we introduce the concept of "chemo-thermal stress" which encompasses both thermal and chemical stresses, to better reflect real-life conditions. Additionally, we examine the influence of microstructural design parameters (solid volume fraction of CAM and the relative density) on the thermal, chemical, and chemo-thermal stresses within the cathode active material and solid electrolyte. Our investigation reveals that the volume change of the cathode active material, a key contributor to induced mechanical stress in ASSBs, does not serve as a reliable criterion for comparing stresses across various materials or types of stress.

This research deliberately excludes the effect of grain sizes of both the cathode active material and the solid electrolyte on mechanical stress, as our previous study demonstrated that induced mechanical stress is independent of the grain sizes of the microstructural components [55].

2. Experimental and simulation methods

2.1. Synthesis of experimental structure

The composite cathode consists of $LiCoO_2$ (LCO) and aluminum and tantalum-substituted LLZO (nominal composition: $Li_{6.45}Al_{0.05}La_3Zr_{1.6}Ta_{0.4}O_{12}$), abbreviated as LLZO, was synthesized with a mass ratio of 2:1 LCO to LLZO, via a modified solid-state reaction (SSR) method as previously described [56,57]. The cathode active materials LCO and NCM955 were purchased from the commercial suppliers MTI Corporation, Richmond, CA, USA and MSE Supplies LLC, Tucson, AZ, USA, respectively.

2.2. Characteristics of the microstructure

The percentage of cathode active material to the total solid phases in the composite cathode denoted by SVF_{CAM} is given by:

$$SVF_{CAM} = \frac{\overline{V}_{CAM}}{\overline{V}_{CAM} + \overline{V}_{LLZO}} \quad (1)$$

Similarly, the ratio of solid electrolyte to the total solid components in the composite cathode denoted by SVF_{LLZO} is given by:

$$SVF_{LLZO} = \frac{\overline{V}_{LLZO}}{\overline{V}_{CAM} + \overline{V}_{LLZO}} \quad (2)$$

Where $\overline{V}_{CAM}$ and $\overline{V}_{LLZO}$ are the volume fraction of cathode active material (LCO, $Li_{0.5}$NCM955and $Li_{0.1}$NCM955) and the volume fraction of the solid electrolyte (LLZO) with respect to the total volume respectively.

The volumetric fraction of the composite cathode's total solid components to the total volume represents the relative density ($\overline{\rho}$), which is given by:

$$\overline{\rho} = \overline{V}_{CAM} + \overline{V}_{LLZO} \quad (3)$$

2.3. Generation of representative volume element

Focused Ion Beam Scanning Electron Microscopy (FIB-SEM) was employed to acquire a stack of SEM images of the cross section with a 50 nm of voxel size. Subsequently, specially developed assorted computer-

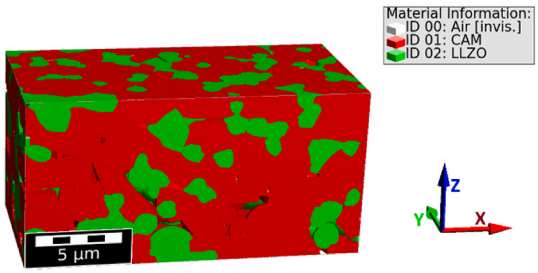

Fig. 1. Regenerated modelled microstructure utilizing cathode active materials (CAM), LCO, $Li_{0.5}$NCM955 or $Li_{0.1}$NCM955. SVF_{CAM} = 69.4 %, initial average grain size of CAM and LLZO are 2.00 µm and 1.43 µm respectively and $\overline{\rho}$ = 93.14 %.

aided methodologies were applied to construct a model representing the experimental configuration. Further exhaustive details regarding this procedural approach can be found in alternative sources [58,59]. During the analysis, a focused examination of material impact was carried out, specifically assessing LCO and NCM955 using identical microstructures. Roitzheim et al. [53] utilized microstructures of NCM/LLZO cathodes, which demonstrated similar porosity to LCO/LLZO cathodes. Their findings showed that replacing LCO with NCM has minimal impact on the cathode microstructure, owing to their similar hexagonal layered structures. Both exhibit size and shape attributes comparable to those of commercially sourced powders.

The composite cathode microstructures were generated using GeoDict software, incorporating a Python script, following a series of steps outlined in Ref. [55]. Initially, grains of composite components (CAM and LLZO) were stacked to fill a domain measuring 400 × 200 × 300 voxels (voxel length = 50 nm) from the positive z-direction. To align with experimental findings [59], hexagonal grains were horizontally oriented (parallel to the Y-axis) within the modelled sample The initial SVF_{CAM} was set at 69.4 %, with average grain diameters of 2.00 µm for CAM and 1.41 µm for LLZO. Subsequently, the distribution step was initiated, ensuring the attainment of a homogenous representative structure. Regions displaying deviations in SVF_{CAM} or lower back densities were removed in the third step, reducing the domain size to 400 × 200 × 200 voxels. The structure was then subjected to sintering using the Voronoi tessellation algorithm implemented in GeoDict [60] to achieve the targeted density value of 93.14 %. If necessary, the first four steps were iterated with adjusted input values for the SVF_{CAM} and the $\overline{\rho}$ to ensure maximum deviations of 0.25 % from the target values. This achieved by utilizing the DFSANE algorithm (derivative-free spectral approach for solving nonlinear systems of equations) [61]. Fig. 1 shows the regenerated modelled microstructure consisting of CAM (LCO, $Li_{0.5}$NCM955 or $Li_{0.1}$NCM955) and LLZO.

2.4. Calculation of stiffness matrix of NCM955

Spin-polarized DFT calculations were then performed using the projector augmented wave (PAW) potential method [62] implemented in the Vienna *Ab Initio* Simulation Package (VASP) code [63]. Generalized gradient approximation (GGA) within the scheme of Perdew–Burke–Ernzerhof (PBE) [64] was chosen as the exchange-correlation functional. To perform DFT calculations for discharged and charged systems, we modelled $Li_xNi_{0.9}Co_{0.05}Mn_{0.05}O_2$ (Li_xNCM955) structure (space group: R-3m) using 4 × 4 × 1 supercells. A gamma-centred *k*-point mesh of 2 × 2 × 2 was applied. An energy cut off of 800 eV as well as electronic and force convergence criteria of 10^{-5} eV and 10^{-3} eV/Å, respectively, were used. For calculating elastic constants *Cij*, we fixed the magnetic moment and atomic coordinates to the optimized ones obtained for the equilibrium lattice parameters. C_{ij} matrix was computed using the strain values of 0, ±0.5 %, and ±1 %.

2.5. Materials parameters

This study had been performed using half lithium concentration of LCO as the input parameter. While LCO, consistent with the behavior of most active materials, exhibits maximum strain at this concentration,

Table 1
Elastic parameters including the anisotropic stiffness matrix C, Young's modulus E, and Poisson ratio ν for the cathode active materials LCO, NCM955, $Li_{0.5}$CO, $Li_{0.5}$NCM955, $Li_{0.1}$NCM955 and the electrolyte material LLZO.

Material	Elastic parameter	Ref
LCO	$C = \begin{bmatrix} 339.79 & 101.6 & 65.78 & -6.39 & 0 & 0 \\ & 339.79 & 65.78 & 0 & 0 & 0 \\ & & 214.67 & 0 & 0 & 0 \\ & sym. & & 51.47 & 0 & 0 \\ & & & & 51.47 & 0 \\ & & & & & 119.095 \end{bmatrix}$ GPa	[65]
NCM955	$C = \begin{bmatrix} 282.62 & 153.1 & 40.75 & 0 & 0 & 0 \\ & 282.62 & 40.75 & 0 & 0 & 0 \\ & & 354.67 & 0 & 0 & 0 \\ & sym. & & 98.79 & 0 & 0 \\ & & & & 98.79 & 0 \\ & & & & & 64.76 \end{bmatrix}$ GPa	
$Li_{0.5}CO_2$	$C = \begin{bmatrix} 303.86 & 101.71 & 32.58 & 0 & 7.31 & 0 \\ & 318.93 & 28.66 & 0 & -3.93 & 0 \\ & & 98.93 & 0 & 7.03 & 0 \\ & sym. & & 18.02 & 0 & -2.46 \\ & & & & 15.73 & 0 \\ & & & & & 101.94 \end{bmatrix}$ GPa	[65]
$Li_{0.5}$NCM955	$C = \begin{bmatrix} 279.1 & 117.8 & 107.7 & 0 & 0 & 0 \\ & 279.1 & 107.7 & 0 & 0 & 0 \\ & & 184.6 & 0 & 0 & 0 \\ & sym. & & 75.2 & 0 & 0 \\ & & & & 75.2 & 0 \\ & & & & & 80.6 \end{bmatrix}$ GPa	[66]
$Li_{0.1}$NCM955	$C = \begin{bmatrix} 278 & 91.5 & 114.2 & 0 & 0 & 0 \\ & 278 & 114.2 & 0 & 0 & 0 \\ & & 158.7 & 0 & 0 & 0 \\ & sym. & & 70.6 & 0 & 0 \\ & & & & 70.6 & 0 \\ & & & & & 93.2 \end{bmatrix}$ GPa	[66]
LLZO	E = 146 GPa, ν = 0.26	[67–69]

Table 2
Crystallographic strains for LCO, $Li_{0.5}$NCM955 and $Li_{0.1}$NCM955 in a-and c-axes and for LLZO, in the as-manufactured state, fully lithiated (ϵ^{Th}), chemically sub-stoichiometric lithium (ϵ^{Li}) and chemo-thermal ($\epsilon^{chemo-thermal}$).

Material	ϵ^{Th}	ϵ^{Li}	$\epsilon^{chemo-thermal}$
$Li_{0.5}CO_2$	$\epsilon^a = -1.53 \times 10^{-2}$ $\epsilon^c = -2.36 \times 10^{-2}$ **($Li_{1.0}CoO_2$)**	$\epsilon^a = -2.3 \times 10^{-3}$ $\epsilon^c = 2.39 \times 10^{-2}$ [59,70,71]	$\epsilon^a = -1.76 \times 10^{-2}$ $\epsilon^c = 2.38 \times 10^{-4}$
$Li_{0.5}$NCM955	$\epsilon^a = -1.91 \times 10^{-2}$ $\epsilon^c = -1.76 \times 10^{-2}$ **($Li_{1.0}$NCM955)**	$\epsilon^a = -1.23 \times 10^{-2}$ $\epsilon^c = 2.81 \times 10^{-2}$ [66]	$\epsilon^a = -3.14 \times 10^{-2}$ $\epsilon^c = 1.04 \times 10^{-2}$
$Li_{0.1}$NCM955	Same as $Li_{0.5}$NCM955	$\epsilon^a = -3.95 \times 10^{-2}$ $\epsilon^c = -3.09 \times 10^{-2}$ [66]	$\epsilon^a = -5.86 \times 10^{-2}$ $\epsilon^c = -4.85 \times 10^{-2}$
LLZO (LCO as CAM)	-1.42×10^{-2}	0	-1.42×10^{-2}
LLZO (NCM955 as CAM)	-1.32×10^{-2}	0	-1.32×10^{-2}

NCM955 behaves differently, in which a higher degree of delithiation is required to achieve maximum strain. Hence, $Li_{0.1}$NCM955 was selected. Additionally, at half the lithium concentration of NCM955, its anisotropic lattice strain shows the largest deviation. The stiffness matrices of the anisotropic materials, Young's moduli and Poisson ratios of the isotropic materials are presented in Table 1. During the cooling stage subsequent to the sintering process, both the cathode active material and LLZO undergo contraction in all directions. Notably, LCO and NCM955 exhibit distinct anisotropic behaviors during this phase. Therefore, an internal thermal stress would be induced ascribed to the difference in coefficient of (α^{Th}) between CAM and LLZO. In-situ high temperature X-ray diffraction (HT-XRD), was utilized to determine the lattice parameters thereby quantifying the thermal strains (ϵ^{Th}) of LCO, NCM955 and LLZO. Temperature variations range from 0 to 1000 °C for LCO and LLZO powders, while for NCM955 the range is limited to 0–900 °C, as our experimental observations revealed decomposition of NCM955 beyond this temperature. This distinction was essential to accurately represent realistic chemo-thermal stress conditions specific to each material. The temperature change rate was maintained at 5 K min^{-1} to ensure precise experimental conditions. Additional information regarding this process is provided in the Supplementary information. The extraction of positive lithium ions during the delithiation of cathode active materials induces chemical strains ($\epsilon^{Chemical}$). For LCO and $Li_{0.5}$NCM955, substantial expansion in c-axis is observed ascribed to the repulsive force between the resulted negative charged layers. Conversely, $Li_{0.1}$NCM955 exhibits contraction along the c-axis.

Furthermore, cathode active materials with layered structure, exhibit contraction along both a and b-axes, which in turn leads to a net volume change of 1.91 %, 0.35 % and −11.0 % for LCO, $Li_{0.5}$NCM955 and $Li_{0.1}$NCM955 respectively. Doped LLZO doesn't exhibit any volume change during delithiation due to the stability of its phase and Li content. The combination of thermal and chemical strains leads to the emergence of chemo-thermal strains ($\epsilon^{Chemo-thermal}$). Its significance lies in its representation of realistic behavior, taking into account both cooling after sintering and delithiation steps. The values of thermal, chemical and chemo-thermal strains for cathode active materials and LLZO are listed in Table 2.

In this study, stress histograms are used to display the differential relative frequency as a function of principal stress values, providing a detailed representation of stress distribution. More information can be found in Ref. [66]. The average of the principal stress $\overline{\boldsymbol{S}}_{\boldsymbol{all}}$, was calculated using the ElastoDict FeelMath-LD module within GeoDict, developed by Math2Market GmbH [72,73]. While the standard deviation **ΔS** represents the width of distribution. Symmetric (Dirichlet) boundary conditions were applied in all directions. Small deformations were considered, as all deformations were within the small-scale range ≤5 %, thereby justifying the use of linear superposition for the calculation of chemo-thermal stress. Phase transformations are implicitly incorporated through the strain-based formulation. Although interfacial reactions may induce the formation of secondary phases, their influence is considered negligible due to their limited extent and the lack of well-characterized material properties for the resulting phases. Consequently, it is reasonable to assume that the initial stress distribution within the grains is not significantly affected by such interfacial phenomena.

2.6. Definition of induced mechanical stress

The principal cause of induced mechanical stress in composite cathodes of ASSBs arise from the volume change of the CAM during delithiation, as well as the volume change in both the CAM and LLZO during the cooling down after sintering. In both instances, LLZO hinders the volume change of the CAM within the system, consequently leading to induced mechanical stress. The determination of volume change relies on the strain values of these components. For CAM, the total strain (ϵ_{CAM}) in one direction (a, b and c-axes) is given by:

$$(\epsilon_{CAM})_i = (\epsilon^{Li}_{CAM})_i + (\epsilon^{Th}_{CAM})_i + (\epsilon^{El}_{CAM})_i \; (i = a, b, c) \quad (4)$$

Where ϵ^{Li}_{CAM}, ϵ^{Th}_{CAM} and ϵ^{El}_{CAM} are the lithiation, thermal and elastic strains of CAM.

On other hand, LLZO has no volume change during cycling, hence, the total strain of LLZO (ϵ_{LLZO}) in given direction (a, b and c-axes) is

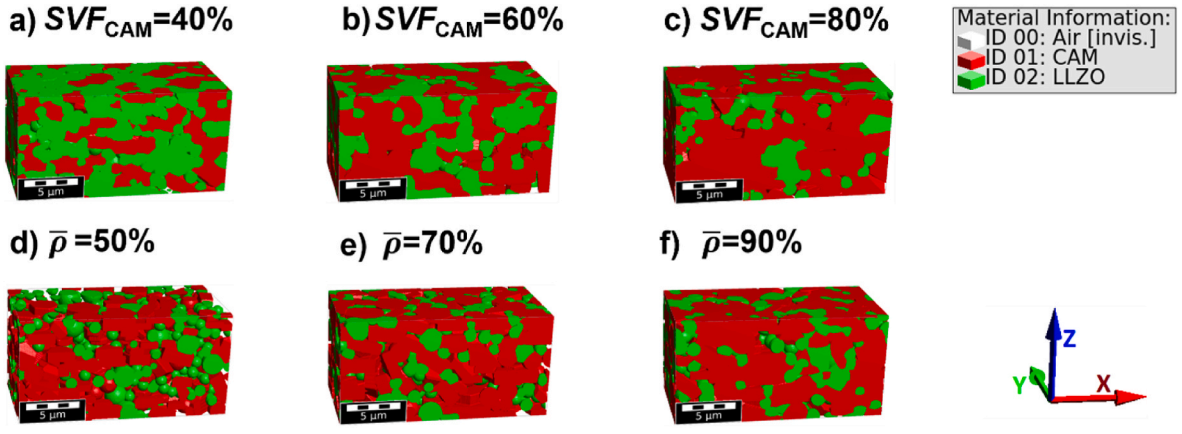

Fig. 2. a-c) Variation of SVF_{CAM} only (40, 60 and 80 %), d-f) variation of $\overline{\rho}$ only (50, 70 and 90 %). The fixed parameters values were as follow: $SVF_{CAM} = 69.4$ %, $\overline{\rho} = 93.14\%$, $d_{CAM} = 2.00$ µm and $d_{LLZO} = 1.41$ µm.

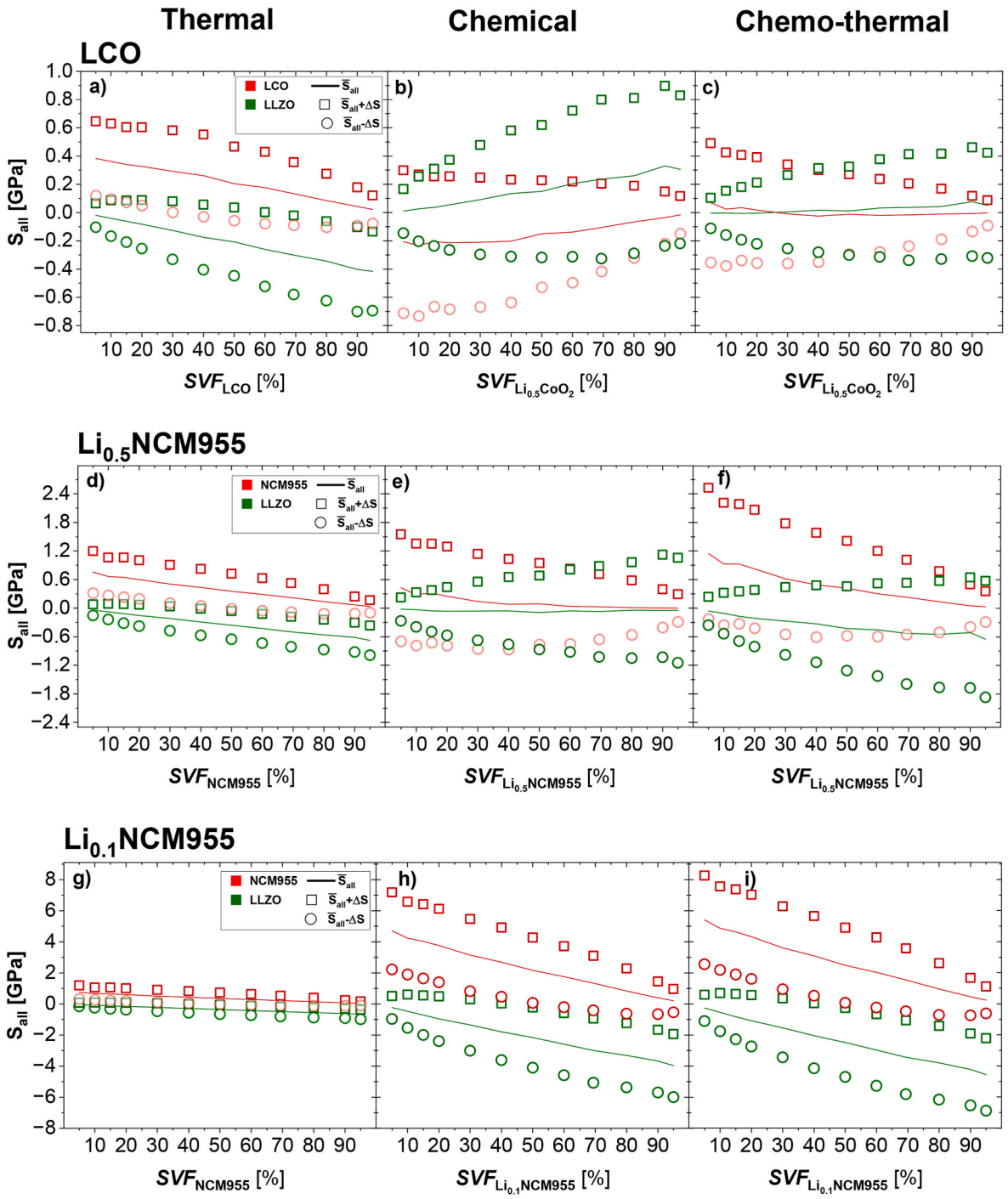

Fig. 3. The impact of SVF_{CAM} on the principal stresses for CAM (LCO a-c, $Li_{0.5}$NCM955 d-f and $Li_{0.1}$NCM955 g-i) and LLZO in case of: a, d and g) thermal, b, e, and h) chemical and c, f and i) chemo-thermal stress. The fixed parameters values were as follow: SVF_{CAM} = 69.4 %, $\bar{\rho}$ = 93.14%, d_{CAM} = 2.00 μm and d_{LLZO} = 1.41 μm.

given by:

$$(\epsilon_{LLZO})_i = (\epsilon^{Th}_{LLZO})_i + (\epsilon^{El}_{LLZO})_i \quad (5)$$

Where ϵ^{Th}_{LLZO} and ϵ^{El}_{LLZO} are the thermal and elastic strains of LLZO phases, respectively.

The elastic strain of CAM and LLZO is linked to the stresses by Hook's law:

$$(\sigma_{CAM})_j = C^{CAM}_{ij}(\epsilon^{El}_{CAM})_i \quad (6)$$

For LLZO:

$$\sigma^i_{LLZO} = E(\epsilon^{El}_{LLZO})_i \quad (7)$$

2.7. Varying microstructural design parameters

One of the primary objectives of this study is to systematically investigate the impact of microstructural design parameters, including SVF_{CAM}, and the porosity on the distribution of mechanical stress in different scenarios (thermal, chemical, and chemo-thermal). Accordingly, each parameter is deliberately adjusted independently while fixing the others, employing a methodology similar to that described in Ref. [55]. Fig. 2 illustrates examples of each variation. The SVF_{CAM}

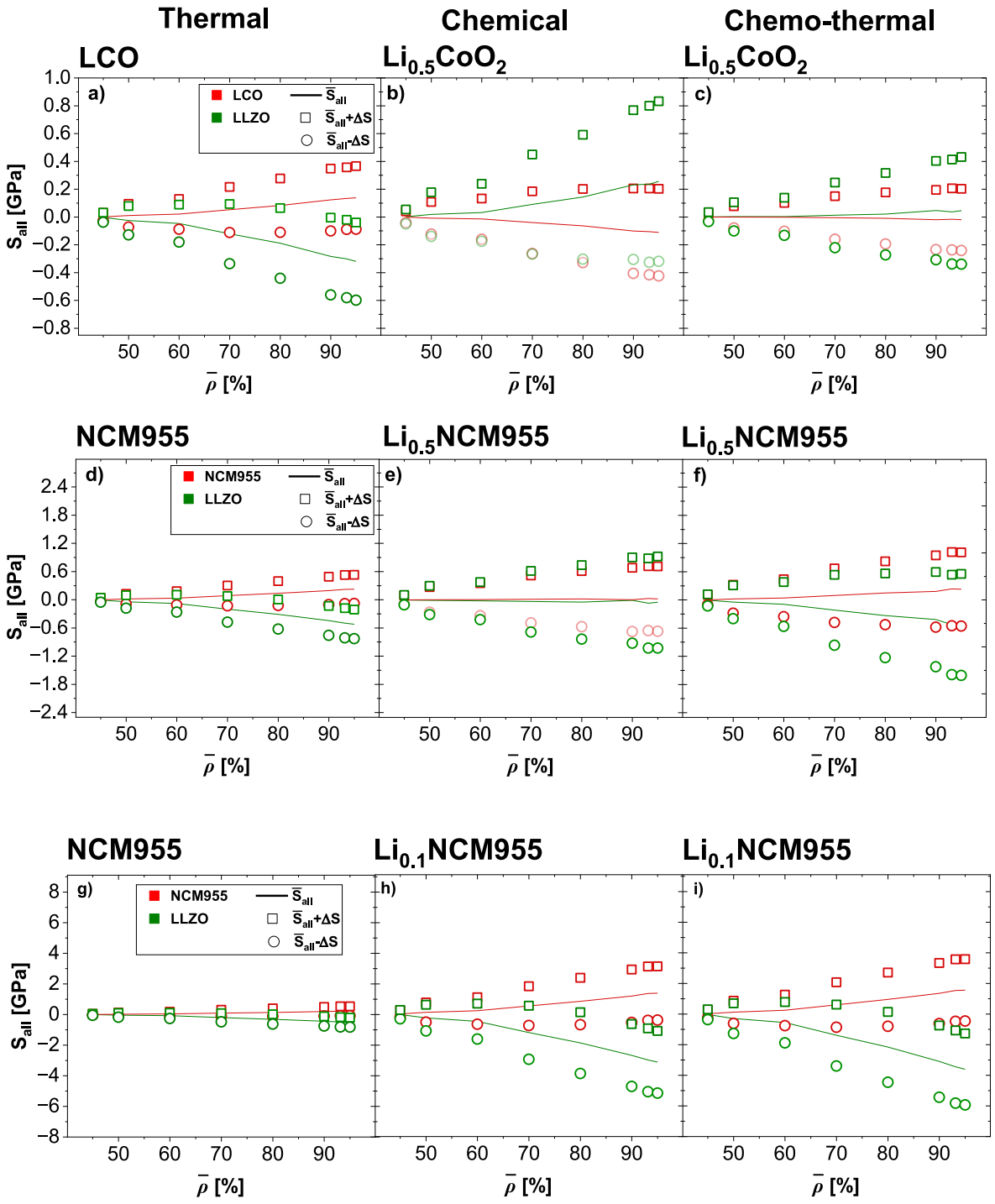

Fig. 4. The impact of $\bar{\rho}$ on the principal stresses for CAM (LCO a-c, $Li_{0.5}$NCM955 d-f and $Li_{0.1}$NCM955 g-i) and LLZO in case of: a, d and g) thermal, b, e and h) chemical and c, f and i) chemo-thermal stress. The fixed parameters values were as follow: SVF_{CAM} = 69.4 %, $\bar{\rho}$ = 93.14%, d_{CAM} = 2.00 μm and d_{LLZO} = 1.41 μm.

ranges from 5 to 95 %, while the percentage of porosity varies from 5 % to 60 %. Subsequently, each set undergoes mechanical characterization. It is noteworthy that the selected range for each parameter exceeds the values observed in experimental cells, extending to extreme values unattainable in real-life scenarios. The practical range of SVF_{CAM} typically falls between 33 % and 66 %. In contrast, the porosity values achieved through unoptimized free sintering range from 30 % to 55 %, whereas for optimized and pressure-assisted sintering, it falls between 5 % and 20 %. The approach used to investigate the effect of a singular microstructural parameter highlights the significant advantages of modeling over experimentation in such research.

3. Results and discussion

3.1. Impact of microstructural design parameters on induced mechanical stress

The influence of microstructural design parameters on mechanical stresses in composite cathodes of ASSBs was investigated. These parameters included SVF_{CAM} and $\bar{\rho}$. The study investigated thermal, chemical, and chemo-thermal stresses, considering scenarios with LCO, $Li_{0.5}$CO, $Li_{0.5}$NCM955, and $Li_{0.1}$NCM955 as CAMs

The parameter governing the cell's capacity is the ratio of active material

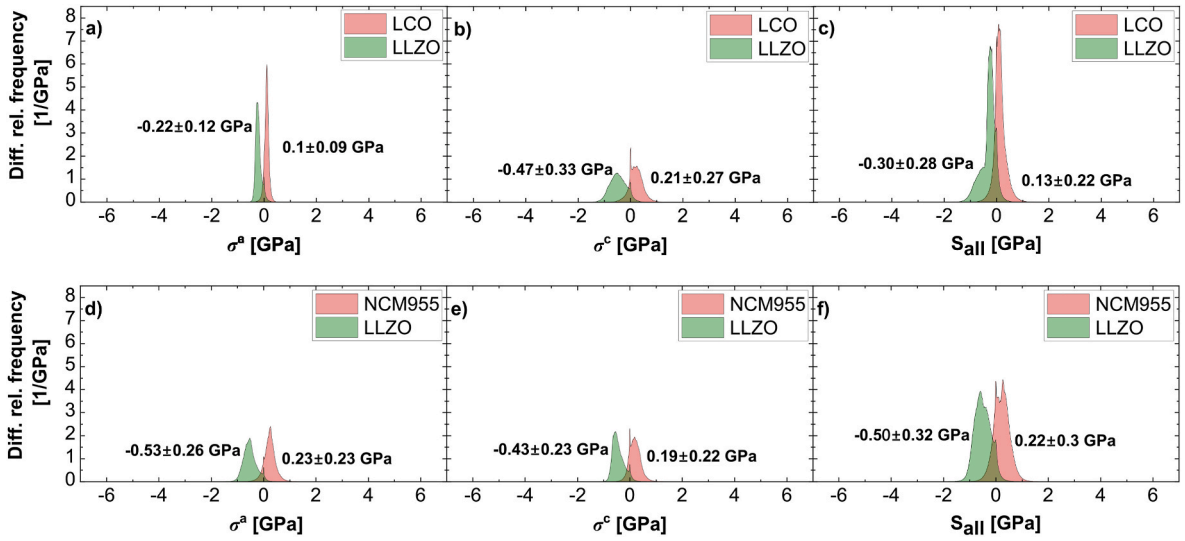

Fig. 5. Thermal principal stress (S_{all}) of LCO and NCM955 in the regenerated modelled microstructure a and d) in a-axis, b and e) in c-axis, c and f) the net principal stress.

to solid electrolyte within the composite cathode. Bulk LLZO materializes when SVF_{CAM} is absent. Hence, stress-free state for LLZO occurred. As the SVF_{CAM} increases, the number of adjacent LLZO grains constraining the volume change of CAM grains decreases, being substituted by CAM grains. This substitution facilitates the volume change of CAM grains, resulting in reduced induced mechanical stress within CAM (Fig. 3a–i). However, the sensitivity of CAM stress to the increase in SVF_{CAM} is relatively low in the range of 5–20 %, ascribed to the insignificant increase in the number of CAM grains within this range due to their relatively larger volume compared to LLZO grains. A notable increase in the number of CAM grains begins at $SVF_{CAM} = 30$ %, leading to higher stress sensitivity to the increase in SVF_{CAM} This is reflected in a significant linear reduction in stress values observed beyond $SVF_{CAM} = 20$ %.

Meanwhile, as SVF_{CAM} increases, the number of LLZO grains significantly decreases. This reduction leads to greater sensitivity of LLZO stress to variations in SVF_{CAM}, characterized by a significant increase in LLZO stress following a continuous linear trend under these conditions (Fig. 3a–i). Bulk CAM is present when the solid volume fraction of solid electrolyte reaches 0 %, leading to the disappearance of LLZO in the framework. Therefore, the constraints of LLZO vanishes leading to stress-free state for aligned CAM.

The percentage of porosity in the structure is represented by $\overline{\rho}$. The existence of residual porosity in the microstructure is essential, as it facilitates the volume change in the cathode active material and introduces a strain tolerance. In the context of a highly porous structure ($\overline{\rho} = 45$ %), LLZO exerts lower constraints on CAM, due to lower coordination number of particles. As a result, a notably diminished mechanical stress is observed.

By increasing $\overline{\rho}$, the mechanical stress of CAM and LLZO exhibits a progressive augmentation due to reduced degree of freedom in volume change for both CAM and LLZO (Fig. 4).

During the thermal scenario, CAM and LLZO experience tensile and compressive stresses, respectively, due to the higher contraction strains of CAM compared to LLZO (Fig. 3a–d and g) and (Fig. 4a–d and g). In contrast, during delithiation, both $Li_{0.5}CO$ and LLZO exhibit stress inversion, with LCO undergoing compressive stress and LLZO experiencing tensile stress (Fig. 3b–e and h) and (Fig. 4b–e and h). On the other hand, $Li_{0.5}NCM955$ continues to experience tensile stress despite its volume expansion, while LLZO undergoes compressive stress during delithiation. This behavior will be discussed in detail in section (3.2.2).

Meanwhile, $Li_{0.1}NCM955$ and LLZO remain under tensile and compressive stresses, respectively, attributed to the higher volume contraction of $Li_{0.1}NCM955$ compared to LLZO.

The stress inversion observed in the $Li_{0.5}CO$/LLZO system persists under chemo-thermal conditions (Fig. 3c–f and i) and (Fig. 4c–f and i), ascribed to the greater volume expansion of $Li_{0.5}CO$ relative to the volume contraction of LLZO. In contrast, both $Li_{0.5}NCM955$/LLZO and $Li_{0.1}NCM955$/LLZO systems maintain their respective stress types during the chemo-thermal case, due to the higher volume contraction of both $Li_{0.5}NCM955$ and $Li_{0.1}NCM955$ compared to that of LLZO.

3.2. Effect of residual thermal stress on the total induced mechanical stress

3.2.1. Thermal stress

During cooling down after sintering, the composite components undergo a contraction along distinct crystallographic axes (a, b, and c-axes), inducing multidirectional shrinkage. Which in turn forming a thermal strain (ϵ^{Th}), with the thermal expansion coefficient serving as a critical parameter.

Thermal strains observed in both LCO and NCM955 are higher than those in LLZO, ascribed to the higher thermal expansion coefficients of LCO and NCM955 compared to LLZO. In essence, LCO and NCM955 exhibit higher sensitivity to thermal treatment relative to LLZO. Consequently, LLZO appears to impede the shrinking of LCO and NCM955, exhibiting a smaller negative volume change compared to the cathode active materials. While this trend is general, it is particularly pronounced in the LCO/LLZO system along the c-axis compared to the a and b-axes. Conversely, in the case of NCM955/LLZO, the effect is more noticeable along both the a and b-axes. Within this framework, both ϵ^{C}_{LCO} and $\epsilon^{a,b}_{LCO}$ exhibit negative sign due to the shrinking process. Resulting a net tensile principal stresses in LCO and compressive principal stress in LLZO along theses axes (Fig. 5a–c). Similar trend and explanation apply for NCM955 (Fig. 5d–f). In our modelled regenerated structure, the overall induced thermal stress of NCM955 S^{NCM955}_{all} is higher than that of LCO S^{LCO}_{all} (0.220 ± 0.30 GPa and 0.13 ± 0.22 GPa), respectively. (Fig. 5f–c).

3.2.2. Chemical stress

The dissipation of LLZO-induced strains during delithiation of the composite cathode is attributed to the absence of volume change within the LLZO phase.

$Li_{0.5}CO$ tends to shrink along a and b-axes inducing mechanical stress ascribed to the constrained LLZO phase which hinders the contraction of $Li_{0.5}CO$ along these axes. The value of the strain change increases with

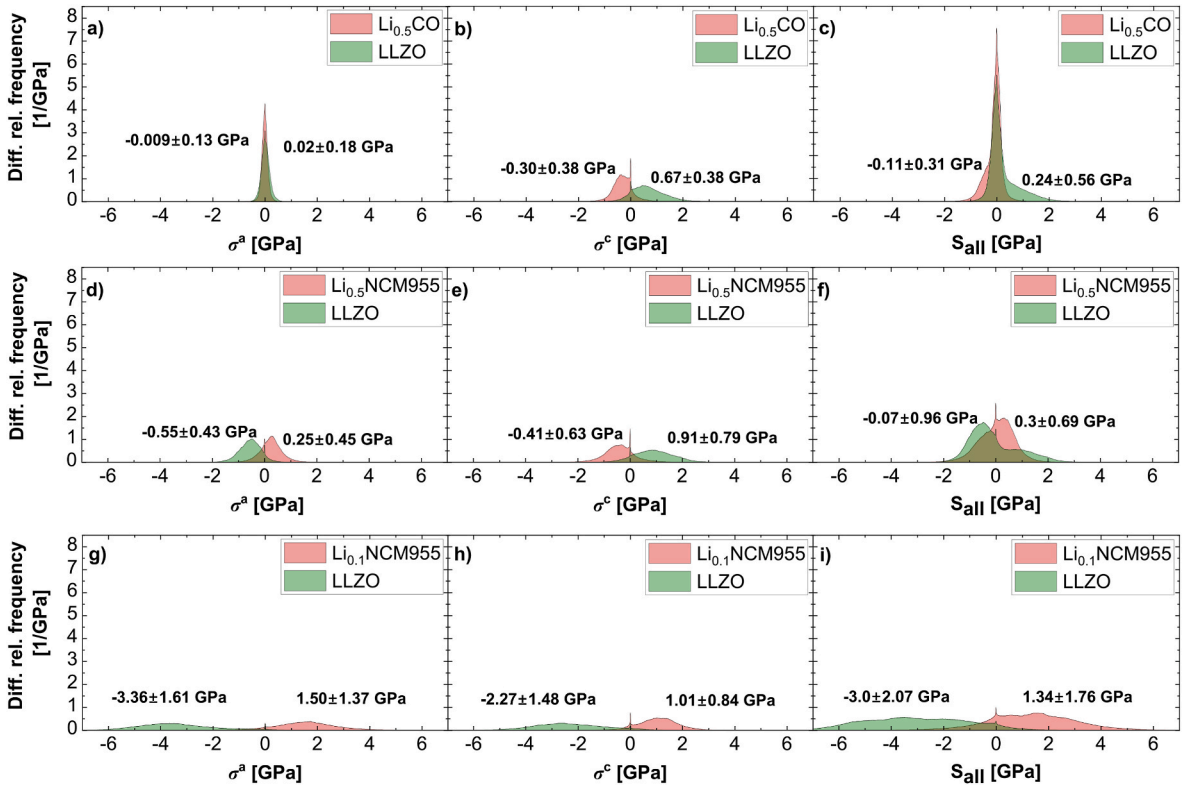

Fig. 6. Chemical principal stress (S_{all}) histogram of LCO $Li_{0.5}$NCM955and $Li_{0.1}$NCM955 in the regenerated modelled microstructure, a, d and g) in a-axis, b, e and h) in c-axis, c, f and i) the net principal stress.

distance from the interface between the cathode active material and LLZO. Leading to positive sign of $\sigma^{a,b}_{LCO}$ indicating very mild tensile principal stresses, while on other hand $\sigma^{a,b}_{LLZO}$ will have negative sign, indicating slight compressive principal stress. (Fig. 6a). The scenario in the c-axis undergoes a complete inversion. Where, LLZO phase restricts the expansion of LCO along this axis, the total strain values of LCO are gradually increased as we move away of the interface between cathode active materials and LLZO, allowing the cathode active materials to freely expand. A similar trend is observed in LLZO. Where, the strain values decrease gradually as we move away from the interface. In this context, ϵ^{C}_{LCO} exhibits positive sign due to the expansion process. Consequently, the sign of σ^{c}_{LCO} will be negative indicating to a compressive principal stress, while the sign of σ^{c}_{LLZO} LLZO will be positive indicating tensile principal stresses in this direction (Fig. 6b). The sign of net principal stress is determined by both the strain in each direction and by the resistance to deformation in each direction. In the LCO/LLZO system, ϵ^{C}_{LCO} is tenfold greater than $\epsilon^{a,b}_{LCO}$. This leads to higher value of σ^{c}_{LCO} compared to $\sigma^{a,b}_{LCO}$, in spite of that C^{C}_{LCO} is about 0.33 times lower than C^{a}_{LCO}. Resulting in a negative sign of S^{LCO}_{all}, indicative of a net compressive principal stress, while S^{LLZO}_{all} will exhibit a positive sign, indicating a net tensile principal stress (Fig. 6c). In our modelled regenerated structure, LCO exhibits a compressive stress of -0.11 ± 0.31 GPa.

Similar behavior is observed in the $Li_{0.5}$NCM955/LLZO system, where the material contracts along both the a and b axes. This contraction induces mechanical stress due to the adjacent LLZO, which impedes the contraction of $Li_{0.5}$NCM955 along these axes. Leading to positive sign of $\sigma^{a,b}_{Li_{0.5}NCM955}$ indicating tensile principal stresses. Conversely, $\sigma^{a,b}_{LLZO}$ exhibits a negative sign, indicating compressive principal stresses. (Fig. 6d). Along the c-axis, the scenario is reversed. The LLZO phase restricts the expansion of $Li_{0.5}$NCM955 along this axis. The strain values in $Li_{0.5}$NCM955 gradually increase with distance from the interface between the cathode active material and LLZO, allowing for free expansion of the cathode material. Similarly, in LLZO, strain values gradually decrease with increasing distance from the interface, leading to negative sign of $\sigma^{c}_{Li_{0.5}NCM955}$ indicating to a compressive principal stress, while the sign of σ^{c}_{LLZO} LLZO is positive indicating to a tensile principal stress in this direction (Fig. 6e). Despite the value of $\epsilon^{C}_{Li_{0.5}NCM955}$ is about 2.3 times higher than $\epsilon^{a,b}_{Li_{0.5}NCM955}$, which in turn leads to a positive volume change in $Li_{0.5}$NCM955 yet, it is not sufficient enough to overcome the partially tensile stress, ascribed to 0.6 times lower $C^{C}_{Li_{0.5}NCM955}$ compared to $C^{a}_{Li_{0.5}NCM955}$, leaving the induced tensile stress along both a and b-axes to be dominant in the system. Consequently, $S^{Li_{0.5}NCM955}_{all}$ will exhibit a positive sign, indicating a net tensile principal stress of 0.32 ± 0.69 GPa, while S^{LLZO}_{all} will have a negative sign, indicating a net compressive principal stress (Fig. 6f). In the $Li_{0.1}$NCM955/LLZO system, $Li_{0.1}$NCM955 shows similar behavior as NCM955 in the thermal case, where it has a negative volume change owed to the contraction of $Li_{0.1}$NCM955 in all directions leading to an induced tensile principal stress in all direction as well (Fig. 6g and h). Consequently, $S^{Li_{0.1}NCM955}_{all}$ will exhibit a positive sign, indicating a net tensile principal stress of 1.34 ± 1.76 GPa for our modelled structure, while S^{LLZO}_{all} exhibits a negative sign, indicating a net compressive principal stress (Fig. 6i).

3.2.3. Chemo-thermal stress

The chemo-thermal stress integrates both thermal and chemical contributions and considers the residual stress from cooling after sintering as well as due to electrochemical cycling.

In the LCO/LLZO system, negative strains are induced in both LCO and LLZO due to contraction during cooling after sintering. These negative strains partially offset the positive strains developed in LCO during delithiation, thus reducing the overall strain and minimizing the strain difference between LCO and LLZO in the chemo-thermal phase.

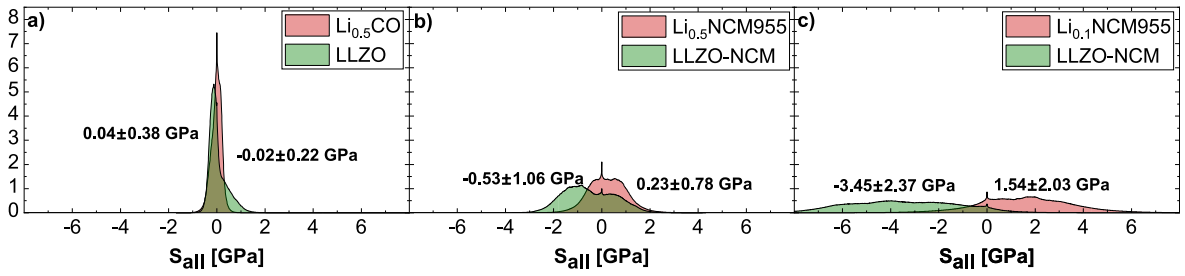

Fig. 7. Chemo-thermal net principal stress (S_{all}) histogram in the regenerated modelled microstructure of a) LCO b) $Li_{0.5}$NCM955, and c) $Li_{0.1}$NCM955.

Our simulation calculations demonstrate that the net induced compressive stress in $Li_{0.5}$CO during the delithiation process surpasses the net induced tensile stress during post-sintering cooling. This results in a reduced overall compressive stress within LCO. Similarly, for LLZO, the net induced tensile stress is reduced (Fig. 3a–c and Fig. 4a–c). Our computational model quantifies the chemo-thermal stress in $Li_{0.5}$CO as -0.02 ± 0.22 GPa (Fig. 7a), approximately 43 % lower than the induced principal stress during delithiation. The behavior differs markedly in systems using $Li_{0.5}$NCM955 and $Li_{0.1}$NCM955 as cathode active materials with LLZO as the solid electrolyte. For $Li_{0.5}$NCM955, our results show that the negative strains induced during cooling down after sintering amplified the dominant negative strains in a and b-axes during delithiation. While on other hand, it reduces the positive strain along the c-axis induced during delithiation, leading to higher strain differences between $Li_{0.5}$NCM955 and LLZO in the chemo-thermal case. While for $Li_{0.1}$NCM955, the negative strains in NCM955 induced during cooling down after sintering amplifies the negative strains induced during delithiation in all axes. Resulting in a higher net strain and, therefore, a greater strain difference between $Li_{0.1}$NCM955 and LLZO in the chemo-thermal case. In these configurations, both the thermal and chemical stresses in the cathode materials are tensile. Consequently, the net tensile chemo-thermal stress in $Li_{0.5}$NCM955 and $Li_{0.1}$NCM955 is substantially higher than the individual thermal or chemical stresses alone (Fig. 3d–i and Fig. 4d–i). Specifically, our models show chemo-thermal stress values of 0.23 ± 0.78 GPa for $Li_{0.5}$NCM955 and 1.50 ± 2.0 GPa for $Li_{0.1}$NCM955 (Fig. 7b and c). The induced principal stress in $Li_{0.5}$NCM955 and $Li_{0.1}$NCM955 during the chemo-thermal case is approximately 42 % and 15 % higher, respectively, than during delithiation. This dominant tensile stress environment within these cathode materials aligns with the higher tensile stresses observed during both electrochemical and thermal processes. While for LLZO, in these systems, the net compressive principal stresses are higher than the thermal and chemical stresses (Fig. 3d–i and Fig. 4d–i).

4. Conclusion

In this paper, we emphasize the critical significance of residual stress after sintering on the overall mechanical stress in all-solid-state batteries (ASSBs), while previous researches primarily focused on chemically-induced mechanical stress during delithiation. Our study addresses this gap by accounting for what we term “chemo-thermal” stress. Our findings demonstrate that for LCO, thermal stress significantly reduces the stress induced during delithiation, resulting in a chemo-thermal stress is approximately **43 % lower** than the delithiation stress alone. In contrast, for both $Li_{0.5}$NCM955 and $Li_{0.1}$NCM955, the chemo-thermal principal stress in $Li_{0.5}$NCM955 approximately 42 % higher when considering delithiation only, ($Li_{0.1}$NCM955 being around 15 % higher). This allows us to introduce the chemo-thermal stress as the worst-case scenario which should be addressed. The use of LCO is more reliable than both $Li_{0.5}$NCM955 and $Li_{0.1}$NCM955 regarding to the mechanical properties. This is not only attributed to its lower chemo-thermal stress, but also to the fact that compressive stresses are less likely to cause failure in oxide materials compared to tensile stresses [66]. Moreover, our results show that CAM volume change is not a reliable indicator for comparing mechanical stresses across materials or stress types. Despite $Li_{0.5}$NCM955 exhibiting a lower positive volume change compared to $Li_{0.5}$CO during delithiation, the induced tensile mechanical stress is even higher than the induced compressive mechanical stress in $Li_{0.5}$CO. Our results confirm the findings from our previous study [55] regarding the effect of microstructural design parameters (SVF_{CAM} and $\bar{\rho}$) on mechanical stress. Specifically, the mechanical stress in composite components is inversely proportional to their SVF and directly proportional to their $\bar{\rho}$.

While this study is limited to numerical modeling, different composite cathode samples will be experimentally fabricated and cycled, followed by ex situ XRD measurements to assess their mechanical stresses and validate the modeling approach.

CRediT authorship contribution statement

Fadi Al-Jaljouli: Writing – review & editing, Writing – original draft, Visualization, Validation, Methodology, Investigation, Formal analysis, Data curation, Conceptualization. **Robert Mücke:** Writing – review & editing, Validation, Supervision, Software, Project administration. **Christoph Roitzheim:** Writing – review & editing. **Yoo Jung Sohn:** Writing – review & editing, Data curation. **Najma Yaqoob:** Writing – review & editing, Data curation. **Martin Finsterbusch:** Writing – review & editing. **Payam Kaghazchi:** Writing – review & editing. **Olivier Guillon:** Writing – review & editing, Supervision, Project administration, Funding acquisition.

Declaration of competing interest

The authors declare the following financial interests/personal relationships which may be considered as potential competing interests: Fadi Al-Jaljouli reports financial support was provided by Federal Ministry of Education and Research of Germany in the framework of the Palestinian-German Science Bridge (PGSB) (BMBF Grant Number 01DH16027). Fadi Al-Jaljouli reports financial support was provided by AdamBatt2 (grant no. 13XP0558A). Fadi Al-Jaljouli reports financial support was provided by Dr. Mariam Al-Jaljouli. Fadi Al-Jaljouli reports financial support was provided by Mr. Khalil Abu Ayyash. Martin Finsterbusch, Christoph Roitzheim reports financial support was provided by FestBatt2-Oxide (grant no. 13XP0434A). Martin Finsterbusch, Christoph Roitzheim, Payam Kaghazchi reports financial support was provided by AdamBatt2 (grant no. 13XP0558A). If there are other authors, they declare that they have no known competing financial interests or personal relationships that could have appeared to influence the work reported in this paper.

Acknowledgements

The financial support provided by the Federal Ministry of Education and Research of Germany in the framework of the Palestinian-German Science Bridge (PGSB) (BMBF Grant Number 01DH16027), FestBatt2-Oxide (grant no. 13XP0434A), AdamBatt2 (grant no. 13XP0558A) and

the financial contributions of Dr. Mariam Al-Jaljouli and Mr. Khalil Abu Ayyash are gratefully acknowledged.

Appendix A. Supplementary data

Supplementary data to this article can be found online at https://doi.org/10.1016/j.jpowsour.2025.237136.

Data availability

Data will be made available on request.

References

[1] M. Finsterbusch, T. Danner, C.-L. Tsai, S. Uhlenbruck, A. Latz, O. Guillon, High capacity garnet-based all-solid-state lithium batteries: fabrication and 3D-microstructure resolved modeling, ACS Appl. Mater. Interfaces 10 (26) (2018) 22329–22339, https://doi.org/10.1021/acsami.8b06705.

[2] R. Miyazaki, G. Yamaguchi, E. Yagi, T. Yoshida, T. Tomita, Enhancement of the Li+ conductivity of Li3AlF6 for stable all-solid-state lithium-ion batteries, Acs Appl. Energ. Mater. 7 (6) (2024) 2533–2541, https://doi.org/10.1021/acsaem.4c00115.

[3] K. Kerman, A. Luntz, V. Viswanathan, Y.-M. Chiang, Z. Chen, Review—practical challenges hindering the development of solid state Li ion batteries, J. Electrochem. Soc. 164 (7) (2017) A1731, https://doi.org/10.1149/2.1571707jes.

[4] J. Janek, W.G. Zeier, A solid future for battery development, Nat. Energy 1 (9) (2016) 1–4, https://doi.org/10.1038/nenergy.2016.141.

[5] T. Yang, J. Zheng, Q. Cheng, Y.Y. Hu, C.K. Chan, Composite polymer electrolytes with $Li_7La_3Zr_2O_{12}$ garnet-type nanowires as ceramic fillers: mechanism of conductivity enhancement and role of doping and morphology, ACS Appl. Mater. Interfaces 9 (26) (2017) 21773–21780, https://doi.org/10.1021/acsami.7b03806.

[6] F. Aguesse, W. Manalastas, L. Buannic, J.M. Lopez del Amo, G. Singh, A. Llordés, J. Kilner, Investigating the dendritic growth during full cell cycling of garnet electrolyte in direct contact with Li metal, ACS Appl. Mater. Interfaces 9 (4) (2017) 3808–3816, https://doi.org/10.1021/acsami.6b13925.

[7] R.H. Basappa, T. Ito, T. Morimura, R. Bekarevich, K. Mitsuishi, H. Yamada, Grain boundary modification to suppress lithium penetration through garnet-type solid electrolyte, J. Power Sources 363 (2017) 145–152, https://doi.org/10.1016/j.jpowsour.2017.07.088.

[8] A. Sharafi, H.M. Meyer, J. Nanda, J. Wolfenstine, J. Sakamoto, Characterizing the Li–$Li_7La_3Zr_2O_{12}$ interface stability and kinetics as a function of temperature and current density, J. Power Sources 302 (2016) 135–139, https://doi.org/10.1016/j.jpowsour.2015.10.053.

[9] S. Wenzel, T. Leichtweiss, D. Krüger, J. Sann, J. Janek, Interphase formation on lithium solid electrolytes—an in situ approach to study interfacial reactions by photoelectron spectroscopy, Solid State Ionics 278 (2015) 98–105, https://doi.org/10.1016/j.ssi.2015.06.001.

[10] P. Bron, B. Roling, S. Dehnen, Impedance characterization reveals mixed conducting interphases between sulfidic superionic conductors and lithium metal electrodes, J. Power Sources 352 (2017) 127–134, https://doi.org/10.1016/j.jpowsour.2017.03.103.

[11] S. Wenzel, S. Randau, T. Leichtweiß, D.A. Weber, J. Sann, W.G. Zeier, J.r. Janek, Direct observation of the interfacial instability of the fast ionic conductor Li10GeP2S12 at the lithium metal anode, Chem. Mater. 28 (7) (2016) 2400–2407, https://doi.org/10.1021/acs.chemmater.6b00610.

[12] A. Bates, S. Mukherjee, N. Schuppert, B. Son, J.G. Kim, S. Park, Modeling and simulation of 2D lithium-ion solid state battery, Int. J. Energy Res. 39 (11) (2015) 1505–1518, https://doi.org/10.1002/er.3344.

[13] G. Bucci, T. Swamy, S. Bishop, B.W. Sheldon, Y.-M. Chiang, W.C. Carter, The effect of stress on battery-electrode capacity, J. Electrochem. Soc. 164 (4) (2017) A645, https://doi.org/10.1149/2.0371704jes.

[14] G. Bucci, T. Swamy, Y.-M. Chiang, W.C. Carter, Modeling of internal mechanical failure of all-solid-state batteries during electrochemical cycling, and implications for battery design, J. Mater. Chem. A 5 (36) (2017) 19422–19430, https://doi.org/10.1039/C7TA03199H.

[15] A. Mukhopadhyay, B.W. Sheldon, Deformation and stress in electrode materials for Li-ion batteries, Prog. Mater. Sci. 63 (2014) 58–116, https://doi.org/10.1016/j.pmatsci.2014.02.001.

[16] Y. He, C. Lu, S. Liu, W. Zheng, J. Luo, Interfacial incompatibility and internal stresses in all-solid-state lithium ion batteries, Adv. Energy Mater. 9 (36) (2019) 1901810, https://doi.org/10.1002/aenm.201901810.

[17] P. Li, Y.B. Zhao, Y.X. Shen, S.H. Bo, Fracture behavior in battery materials, JPhys Energy 2 (2) (2020), https://doi.org/10.1088/2515-7655/ab83e1.

[18] J. Auborn, Y. Barberio, Lithium intercalation cells without metallic lithium: and, J. Electrochem. Soc. 134 (3) (1987) 638, https://doi.org/10.1149/1.2100521.

[19] T. Nagaura, K. Tozawa, Progress in Batteries and Solar Cells, vol. 9, JEC Press, 1990, p. 209, https://doi.org/10.1541/ieejfms1990.115.4_349.

[20] B. Wang, J. Bates, F. Hart, B. Sales, R. Zuhr, J. Robertson, Characterization of thin-film rechargeable lithium batteries with lithium cobalt oxide cathodes, J. Electrochem. Soc. 143 (10) (1996) 3203, https://doi.org/10.1149/1.1837188.

[21] A. Kannan, L. Rabenberg, A. Manthiram, High capacity surface-modified LiCoO2 cathodes for lithium-ion batteries, Electrochem. Solid. St 6 (1) (2002) A16, https://doi.org/10.1149/1.1526782.

[22] Y.J. Kim, H. Kim, B. Kim, D. Ahn, J.-G. Lee, T.-J. Kim, D. Son, J. Cho, Y.-W. Kim, B. Park, Electrochemical stability of thin-film LiCoO2 cathodes by aluminum-oxide coating, Chem. Mater. 15 (7) (2003) 1505–1511, https://doi.org/10.1021/cm0201403.

[23] C. Daniel, D. Mohanty, J. Li, D.L. Wood, Cathode materials review, AIP Conf. Proc. 1597 (1) (2014) 26–43, https://doi.org/10.1063/1.4878478.

[24] C. Wang, G. Bai, X. Liu, Y. Li, Favorable electrochemical performance of LiMn2O4/LiFePO4 composite electrodes attributed to composite solid electrolytes for all-solid-state lithium batteries, Langmuir 37 (7) (2021) 2349–2354, https://doi.org/10.1021/acs.langmuir.0c03274.

[25] S. Klein, P. Bärmann, T. Beuse, K. Borzutzki, J.E. Frerichs, J. Kasnatscheew, M. Winter, T. Placke, Exploiting the degradation mechanism of NCM523 graphite lithium-ion full cells operated at high voltage, ChemSusChem 14 (2) (2021) 595–613, https://doi.org/10.1002/cssc.202002113.

[26] J.-P. Hu, H. Sheng, Q. Deng, Q. Ma, J. Liu, X.-W. Wu, J.-J. Liu, Y.-P. Wu, High-rate layered cathode of lithium-ion batteries through regulating three-dimensional agglomerated structure, Energies 13 (7) (2020) 1602, https://doi.org/10.3390/en13071602.

[27] L. de Biasi, A.O. Kondrakov, H. Geßwein, T. Brezesinski, P. Hartmann, J.r. Janek, Between scylla and charybdis: balancing among structural stability and energy density of layered NCM cathode materials for advanced lithium-ion batteries, J. Phys. Chem. C 121 (47) (2017) 26163–26171, https://doi.org/10.1021/acs.jpcc.7b06363.

[28] Y.-K. Sun, High-capacity layered cathodes for next-generation electric vehicles, ACS Energy Lett. 4 (5) (2019) 1042–1044, https://doi.org/10.1021/acsenergylett.9b00652.

[29] X. Yan, L. Zhang, J. Lu, Improve safety of high energy density LiNi1/3Co1/3Mn1/3O2/graphite battery using organosilicon electrolyte, Electrochim. Acta 296 (2019) 149–154, https://doi.org/10.1016/j.electacta.2018.11.036.

[30] J.-H. Kim, K.-J. Park, S.J. Kim, C.S. Yoon, Y.-K. Sun, A method of increasing the energy density of layered Ni-rich Li[Ni1−2xCoxMnx]O2 cathodes (x = 0.05, 0.1, 0.2), J. Mater. Chem. A 7 (6) (2019) 2694–2701, https://doi.org/10.1039/C8TA10438G.

[31] Z. Lu, D.D. MacNeil, J.R. Dahn, Layered cathode materials Li [Nix Li (1/3 − 2x/3) Mn (2/3 − x/3)] O 2 for lithium-ion batteries, Electrochem. Solid State Lett. 4 (11) (2001) A191, https://doi.org/10.1149/1.1407994.

[32] N. Yabuuchi, T. Ohzuku, Novel lithium insertion material of LiCo1/3Ni1/3Mn1/3O2 for advanced lithium-ion batteries, J. Power Sources 119–121 (2003) 171–174, https://doi.org/10.1016/S0378-7753(03)00173-3.

[33] W. Li, B. Song, A. Manthiram, High-voltage positive electrode materials for lithium-ion batteries, Chem. Soc. Rev. 46 (10) (2017) 3006–3059, https://doi.org/10.1039/C6CS00875E.

[34] A. Manthiram, J.C. Knight, S.T. Myung, S.M. Oh, Y.K. Sun, Nickel-rich and lithium-rich layered oxide cathodes: progress and perspectives, Adv. Energy Mater. 6 (1) (2016) 1501010, https://doi.org/10.1002/aenm.201501010.

[35] Y. Xi, Y. Liu, D. Zhang, S. Jin, R. Zhang, M. Jin, Comparative study of the electrochemical performance of LiNi0.5Co0.2Mn0.3O2 and LiNi0.8Co0.1Mn0.1O2 cathode materials for lithium ion batteries, Solid State Ionics 327 (2018) 27–31, https://doi.org/10.1016/j.ssi.2018.10.020.

[36] J. Gong, Q. Wang, J. Sun, Thermal analysis of nickel cobalt lithium manganese with varying nickel content used for lithium ion batteries, Thermochim. Acta 655 (2017) 176–180, https://doi.org/10.1016/j.tca.2017.06.022.

[37] X. Liu, X. Wang, B. Yue, G. Liu, W. Yu, X. Dong, J. Wang, Preparation of hierarchical LiNixCoyMnzO2 from solvothermal [NixCoyMnz](OH) 2 via regulating the ratio of Ni, Co, and Mn and its excellent properties for lithium-ion battery cathode, J. Chin. Chem. Soc. 67 (11) (2020) 2062–2070, https://doi.org/10.1002/jccs.202000051.

[38] J. Oh, J. Kim, Y.M. Lee, D.O. Shin, J.Y. Kim, Y.-G. Lee, K.M. Kim, High-rate cycling performance and surface analysis of LiNi1-xCox/2Mnx/2O2 (x=2/3, 0.4, 0.2) cathode materials, Mater, Chem. Phys. 222 (2019) 1–10, https://doi.org/10.1016/j.matchemphys.2018.09.076.

[39] Y. Duan, S.-P. Chen, L. Zhang, L. Guo, F.-N. Shi, Review on oxygen release mechanism and modification strategy of nickel-rich NCM cathode materials for lithium-ion batteries: recent advances and future directions, Energy Fuel. 38 (7) (2024) 5607–5631, https://doi.org/10.1021/acs.energyfuels.3c04636.

[40] R. Murugan, V. Thangadurai, W. Weppner, Fast lithium ion conduction in garnet-type Li7La3Zr2O12, Angew Chem. Int. Ed. Engl. – 46 (41) (2007) 7778, https://doi.org/10.1002/anie.200701144.

[41] C.-L. Tsai, E. Dashjav, E.-M. Hammer, M. Finsterbusch, F. Tietz, S. Uhlenbruck, H. P. Buchkremer, High conductivity of mixed phase Al-substituted $Li_7La_3Zr_2O_{12}$, J. Electroceram. 35 (1) (2015) 25–32, https://doi.org/10.1007/s10832-015-9988-7.

[42] H. Buschmann, J. Dölle, S. Berendts, A. Kuhn, P. Bottke, M. Wilkening, P. Heitjans, A. Senyshyn, H. Ehrenberg, A. Lotnyk, Structure and dynamics of the fast lithium ion conductor “Li 7 La 3 Zr 2 O 12”, Phys. Chem. Chem. Phys. 13 (43) (2011) 19378–19392, https://doi.org/10.1039/C1CP22108F.

[43] C.-L. Tsai, V. Roddatis, C.V. Chandran, Q. Ma, S. Uhlenbruck, M. Bram, P. Heitjans, O. Guillon, $Li_7La_3Zr_2O_{12}$ interface modification for Li dendrite prevention, ACS Appl. Mater. Interfaces 8 (16) (2016) 10617–10626, https://doi.org/10.1021/acsami.6b00831.

[44] F. Yonemoto, A. Nishimura, M. Motoyama, N. Tsuchimine, S. Kobayashi, Y. Iriyama, Temperature effects on cycling stability of Li plating/stripping on Ta-

doped Li7La3Zr2O12, J. Power Sources 343 (2017) 207–215, https://doi.org/10.1016/j.jpowsour.2017.01.009.
[45] C.A. Geiger, E. Alekseev, B. Lazic, M. Fisch, T. Armbruster, R. Langner, M. Fechtelkord, N. Kim, T. Pettke, W. Weppner, Crystal chemistry and stability of "Li7La3Zr2O12" garnet: a fast lithium-ion conductor, Inorg. Chem. 50 (3) (2011) 1089–1097, https://doi.org/10.1021/ic101914e.
[46] G. Larraz, A. Orera, M. Sanjuán, Cubic phases of garnet-type Li 7 La 3 Zr 2 O 12: the role of hydration, J. Mater. Chem. A 1 (37) (2013) 11419–11428, https://doi.org/10.1039/C3TA11996C.
[47] L. Miara, A. Windmüller, C.-L. Tsai, W.D. Richards, Q. Ma, S. Uhlenbruck, O. Guillon, G. Ceder, About the compatibility between high voltage spinel cathode materials and solid oxide electrolytes as a function of temperature, ACS Appl. Mater. Interfaces 8 (40) (2016) 26842–26850, https://doi.org/10.1021/acsami.6b09059.
[48] Y. Ren, T. Liu, Y. Shen, Y. Lin, C.-W. Nan, Chemical compatibility between garnet-like solid state electrolyte $Li_{6.75}La_3Zr_{1.75}Ta_{0.25}O_{12}$ and major commercial lithium battery cathode materials, J. Materiom. 2 (3) (2016) 256–264, https://doi.org/10.1016/j.jmat.2016.04.003.
[49] S. Uhlenbruck, J. Dornseiffer, S. Lobe, C. Dellen, C.-L. Tsai, B. Gotzen, D. Sebold, M. Finsterbusch, O. Guillon, Cathode-electrolyte material interactions during manufacturing of inorganic solid-state lithium batteries, J. Electroceram. 38 (2) (2017) 197–206, https://doi.org/10.1007/s10832-016-0062-x.
[50] L.J. Miara, W.D. Richards, Y.E. Wang, G. Ceder, First-principles studies on cation dopants and Electrolyte|Cathode interphases for lithium garnets, Chem. Mater. 27 (11) (2015) 4040–4047, https://doi.org/10.1021/acs.chemmater.5b01023.
[51] N. Zhang, X. Long, Z. Wang, P. Yu, F. Han, J. Fu, G. Ren, Y. Wu, S. Zheng, W. Huang, C. Wang, H. Li, X. Liu, Mechanism study on the interfacial stability of a lithium garnet-type oxide electrolyte against cathode materials, ACS Appl. Energy Mater. 1 (11) (2018) 5968–5976, https://doi.org/10.1021/acsaem.8b01035.
[52] K.J. Kim, M. Balaish, M. Wadaguchi, L. Kong, J.L.M. Rupp, Solid-state Li–metal batteries: challenges and horizons of oxide and sulfide solid electrolytes and their interfaces, Adv. Energy Mater. 11 (1) (2021) 2002689, https://doi.org/10.1002/aenm.202002689.
[53] C. Roitzheim, Y.J. Sohn, L.-Y. Kuo, G. Häuschen, M. Mann, D. Sebold, M. Finsterbusch, P. Kaghazchi, O. Guillon, D. Fattakhova-Rohlfing, All-solid-state Li batteries with NCM–garnet-based composite cathodes: the impact of NCM composition on material compatibility, Acs Appl. Energ. Mater. 5 (6) (2022) 6913–6926, https://doi.org/10.1021/acsaem.2c00533.
[54] A. Bauer, C. Roitzheim, S. Lobe, Y.J. Sohn, D. Sebold, W.S. Scheld, M. Finsterbusch, O. Guillon, D. Fattakhova-Rohlfing, S. Uhlenbruck, Impact of Ni–Mn–Co–Al-based cathode material composition on the sintering with garnet solid electrolytes for all-solid-state batteries, Chem. Mater. 35 (21) (2023) 8958–8968, https://doi.org/10.1021/acs.chemmater.3c01573.
[55] F. Al-Jaljouli, R. Mücke, P. Kaghazchi, Y.J. Sohn, M. Finsterbusch, D. Fattakhova-Rohlfing, O. Guillon, Microstructural parameters governing the mechanical stress and conductivity of all-solid-state lithium-ion-battery cathodes, J. Energy Storage 68 (2023) 107784, https://doi.org/10.1016/j.est.2023.107784.
[56] M. Mann, M. Küpers, G. Häuschen, M. Finsterbusch, D. Fattakhova-Rohlfing, O. Guillon, The influence of hafnium impurities on the electrochemical performance of tantalum substituted $Li_7La_3Zr_2O_{12}$ solid electrolytes, Ionics 28 (1) (2022) 53–62, https://doi.org/10.1007/s11581-021-04300-w.
[57] M. Mann, M. Küpers, G. Häuschen, M. Finsterbusch, D. Fattakhova-Rohlfing, O. Guillon, Evaluation of scalable synthesis methods for aluminum-substituted Li7La3Zr2O12 solid electrolytes, Materials 14 (22) (2021) 6809, https://doi.org/10.3390/ma14226809.
[58] Z.D. Hood, Y. Zhu, L.J. Miara, W.S. Chang, P. Simons, J.L.M. Rupp, A sinter-free future for solid-state battery designs, Energy Environ. Sci. 15 (7) (2022) 2927–2936, https://doi.org/10.1039/D2EE00279E.
[59] R. Mücke, M. Finsterbusch, P. Kaghazchi, D. Fattakhova-Rohlfing, O. Guillon, Modelling electro-chemical induced stresses in all-solid-state batteries: anisotropy effects in cathodes and cell design optimisation, J. Power Sources 489 (2021) 229430, https://doi.org/10.1016/j.jpowsour.2020.229430.
[60] M. Tanemura, T. Ogawa, N. Ogita, A new algorithm for three-dimensional Voronoi tessellation, J. Comput. Phys. 51 (2) (1983) 191–207, https://doi.org/10.1016/0021-9991(83)90087-6.
[61] R. Varadhan, P. Gilbert, BB: an R package for solving a large system of nonlinear equations and for optimizing a high-dimensional nonlinear objective function, J. Stat. Software 32 (2010) 1–26, https://doi.org/10.18637/jss.v032.i04.
[62] P.E. Blöchl, Projector augmented-wave method, Phys. Rev. B 50 (24) (1994) 17953–17979, https://doi.org/10.1103/PhysRevB.50.17953.
[63] G. Kresse, J. Furthmüller, Efficient iterative schemes for ab initio total-energy calculations using a plane-wave basis set, Phys. Rev. B 54 (16) (1996) 11169–11186, https://doi.org/10.1103/PhysRevB.54.11169.
[64] J.P. Perdew, K. Burke, M. Ernzerhof, Generalized gradient approximation made simple, Phys. Rev. Lett. 77 (18) (1996) 3865–3868, https://doi.org/10.1103/PhysRevLett.77.3865.
[65] S. Yamakawa, N. Nagasako, H. Yamasaki, T. Koyama, R. Asahi, Phase-field modeling of stress generation in polycrystalline $LiCoO_2$, Solid State Ionics 319 (2018) 209–217, https://doi.org/10.1016/j.ssi.2018.02.013.
[66] R. Mücke, N. Yaqoob, M. Finsterbusch, F. Al-Jaljouli, P. Kaghazchi, D. Fattakhova-Rohlfing, O. Guillon, Modelling electro-chemically induced stresses in all-solid-state batteries: screening electrolyte and cathode materials in composite cathodes, J. Mater. Chem. A 11 (35) (2023) 18801–18810, https://doi.org/10.1039/D3TA01729J.
[67] A.-N. Wang, J.F. Nonemacher, G. Yan, M. Finsterbusch, J. Malzbender, M. Krüger, Mechanical properties of the solid electrolyte Al-substituted Li7La3Zr2O12 (LLZO) by utilizing micro-pillar indentation splitting test, J. Eur. Ceram. Soc. 38 (9) (2018) 3201–3209, https://doi.org/10.1016/j.jeurceramsoc.2018.02.032.
[68] J.E. Ni, E.D. Case, J.S. Sakamoto, E. Rangasamy, J.B. Wolfenstine, Room temperature elastic moduli and Vickers hardness of hot-pressed LLZO cubic garnet, J. Mater. Sci. 47 (23) (2012) 7978–7985, https://doi.org/10.1007/s10853-012-6687-5.
[69] S. Yu, R.D. Schmidt, R. Garcia-Mendez, E. Herbert, N.J. Dudney, J.B. Wolfenstine, J. Sakamoto, D.J. Siegel, Elastic properties of the solid electrolyte Li7La3Zr2O12 (LLZO), Chem. Mater. 28 (1) (2016) 197–206, https://doi.org/10.1021/acs.chemmater.5b03854.
[70] X. Wang, I. Loa, K. Kunc, K. Syassen, M. Amboage, Effect of pressure on the structural properties and Raman modes of ${\mathrm{LiCoO}}_{2, Phys. Rev. B 72 (22) (2005) 224102, https://doi.org/10.1103/PhysRevB.72.224102.
[71] Y. Takahashi, N. Kijima, K. Dokko, M. Nishizawa, I. Uchida, J. Akimoto, Structure and electron density analysis of electrochemically and chemically delithiated $LiCoO_2$ single crystals, J. Solid State Chem. 180 (1) (2007) 313–321, https://doi.org/10.1016/j.jssc.2006.10.018.
[72] H. Moulinec, P. Suquet, A numerical method for computing the overall response of nonlinear composites with complex microstructure, Comput. Methods Appl. Mech. Eng. 157 (1–2) (1998) 69–94, https://doi.org/10.1016/S0045-7825(97)00218-1.
[73] M. Schneider, F. Ospald, M. Kabel, Computational homogenization of elasticity on a staggered grid, Int. J. Numer. Methods Eng. 105 (9) (2016) 693–720, https://doi.org/10.1002/nme.5008.